Published in final edited form as:
Nat Geosci. 2018 September ; 11(9): 635–639. doi:10.1038/s41561-018-0203-8.

Magnetite Authigenesis and the Warming of Early Mars

Nicholas J. Tosca[1,*], **Imad A.M. Ahmed**[1], **Benjamin M. Tutolo**[2], **Alice Ashpitel**[1], and **Joel A. Hurowitz**[3]

[1]Dept. of Earth Sciences, University of Oxford, South Parks Road, Oxford, OX1 3AN, UK.

[2]Department of Geoscience, University of Calgary, Calgary, AB, T2N 1N4, Canada

[3]Department of Geosciences, Stony Brook University, Stony Brook, NY 11794-2100, USA.

Abstract

The *Curiosity* rover has documented lacustrine sediments at Gale Crater, but how liquid water became physically stable on the early Martian surface is a matter of significant debate. To constrain the composition of the early Martian atmosphere during sediment deposition, we experimentally investigated the nucleation and growth kinetics of authigenic Fe-minerals in Gale Crater mudstones. Experiments show that pH variations within anoxic basaltic waters trigger a series of mineral transformations that rapidly generate magnetite and $H_2(aq)$. Magnetite continues to form through this mechanism despite high P_{CO2} and supersaturation with respect to Fe-carbonate minerals. Reactive transport simulations that incorporate these experimental data show that groundwater infiltration into a lake equilibrated with a CO_2-rich atmosphere can trigger the production of both magnetite and $H_2(aq)$ in the mudstones. $H_2(aq)$, generated at concentrations that would readily exsolve from solution, is capable of increasing annual mean surface temperatures above freezing in CO_2-dominated atmospheres. We therefore suggest that magnetite authigenesis could have provided a short-term feedback for stabilizing liquid water, as well as a principal feedstock for biologically relevant chemical reactions, at the early Martian surface.

Keywords

Martian atmosphere; Mars Science Laboratory; redox; carbon dioxide; hydrogen

In 2013, NASA's Mars Science Laboratory Curiosity rover discovered an ancient fluvio-lacustrine environment in Gale Crater, Mars. Sedimentological, stratigraphic, and geochemical relationships document a freshwater lake that persisted at Gale crater for hundreds to thousands of years[1,2]. Minerals, such as magnetite, and other compounds preserved in lacustrine mudstones, reflect redox-gradients and neutral to alkaline pH conditions within sediment pore waters during and soon after deposition[3-7]. The paleo-

*Correspondence to: nick.tosca@earth.ox.ac.uk.

Author Contributions: N.J.T. and J.A.H. conceived the research, N.J.T., I.A.M.A., and A.A. performed the laboratory work, B.M.T. developed and executed the reactive transport calculations, and all authors analyzed the data. N.J.T. wrote the paper with contributions from J.A.H., I.A.M.A, and B.M.T.

Competing financial interests: The authors declare no competing financial interests.

environment captured by these deposits shares a distinct set of physical and chemical characteristics with some lake systems on the modern Earth, enabling detailed comparisons between the terrestrial and Martian sedimentary records of planetary habitability[1,2].

Nevertheless, the climate conditions that stabilized liquid water at Gale Crater are unknown. Although CO_2 is widely thought to have dominated the early Martian atmosphere[8], the Curiosity rover has only detected carbonate minerals at abundances significantly less than 1 wt. %[3-6]. At the same time, climate models demonstrate that without additional gases, CO_2-rich atmospheres could not have maintained surface temperatures above freezing[9-10]. S-bearing volcanic species were previously thought to trigger greenhouse warming[11-13], but recent models show that S outgassing would have cooled the Martian surface rather than warming it14,15. In the presence of elevated CO_2, low abundances of H_2 and its reaction products (i.e., CH_4) could have generated sufficient warming to stabilize liquid water[16,17], but plausible generation and delivery mechanisms for these species have remained elusive. For example, volcanic outgassing has been identified as a potential source of H_2[16], but requires mantle redox states that would have limited CO_2 release[18]. Although serpentinization has been implicated as a potential H_2 source on early Mars[19], orbital data indicate that serpentine is rare in Martian bedrock[20]. In addition, because H_2 production from terrestrial seafloor-hosted hydrothermal systems is controlled by a variety of kinetic factors[21-22], the H_2-generating efficiency of Martian settings is poorly understood.

To constrain atmospheric composition at the time mudstones were deposited at Gale Crater, we experimentally simulated chemical processes that formed new, or authigenic, minerals soon after deposition. Comparing our experimental data with geological observations reveals that magnetite precipitation was likely triggered by the infiltration of groundwater into a lake equilibrated with a CO_2-rich atmosphere. Experimental data also show that magnetite precipitation in Gale Crater mudstones would have been accompanied by the production of H_2. Because H_2 and its reaction products can raise annual mean surface temperatures above freezing in CO_2-dominated atmospheres[17], magnetite authigenesis could have provided a short-term feedback mechanism for stabilizing liquid water once climate conditions allowed it to infiltrate surface and subsurface reservoirs. We also show that geological observations by the *Curiosity* rover are consistent with both estimated timescales and predicted climatic shifts associated with transient H_2-induced warming.

Experimental evidence

Reconstructing atmospheric composition from sedimentary rocks requires constraints on authigenic mineral formation pathways. The delivery of Fe^{2+}, Mg^{2+}, and $SiO_2(aq)$ to lake or sediment pore waters would have set the stage for mineral authigenesis as basaltic sediment was deposited, while increases in pH would have established the supersaturation necessary to precipitate authigenic minerals (Supplementary Text; Supplementary Figure 1). Under anoxic conditions (reflected, for example, by the preservation of detrital sulfides in some mudstones[3]), Fe(II)-silicate, -oxide, or -carbonates all become supersaturated if pH increases in mudstone pore waters (Supplementary Text; Supplementary Figure 1). However, a poor understanding of Fe(II)-mineral precipitation kinetics, including the origin of magnetite in Gale Crater mudstones, prohibits robust constraints on atmospheric composition[23, 24, 25].

We addressed these uncertainties with two experimental approaches. First, to investigate the nucleation and growth kinetics of authigenic Fe(II)-minerals in Gale Crater mudstones, we conducted precipitation experiments using synthetic Fe^{2+}, Mg^{2+}, and $SiO_2(aq)$-bearing waters, modeled after those expected to form from reactions between water and basalt (Supplementary Text; Supplementary Figure 2). Experiments show that as these anoxic waters experience pH increases above ~8.0, Fe^{2+} is withdrawn from solution, with minor decreases in Mg^{2+} and $SiO_2(aq)$ (Supplementary Figures 3 and 4). The loss of Fe^{2+} corresponds to a rapid decrease in the oxidation-reduction potential (ORP) of the system to values below the thermodynamic stability of $H_2O(l)$ at standard state conditions (Fig. 1A). This results from the production of reduced electro-active aqueous species during the initial stages of the experiments. The production of these species is transient, subsiding after several hours with a slow return to initial ORP values (Fig. 1A).

Solid phases extracted from the experiments show that increases in pH trigger the nucleation of $Fe(OH)_2$ (Fig. 1B). Once precipitated, ageing of $Fe(OH)_2$ at alkaline pH renders it unstable, even under strictly anoxic conditions; in minutes, $Fe(OH)_2$ rapidly transforms to green rust, a structurally related Fe(II)-Fe(III)-hydroxide (Supplementary Text; Supplementary Figure 5). As pH and strictly anoxic conditions are maintained, green rust transforms to magnetite in several days (Fig. 1B; Supplementary Text; Supplementary Figures 2 & 6).

Because the decomposition of $Fe(OH)_2$ is correlated with the production of reduced species during the first few hours of the experiments, the species must originate by accepting electrons from $Fe(OH)_2$ as it transforms to green rust. The only aqueous species capable of forcing ORP below the thermodynamic stability limit of liquid H_2O is dissolved H_2 gas, which we have identified in our experiments at μmol/kg concentration (Supplementary Text). Once $Fe(OH)_2$ is transformed to green rust, H_2 production ceases and ORP recovers to pre-experiment values as H_2 exsolves to the reactor headspace (Fig. 1A).

To investigate the influence of dissolved CO_2 on authigenic Fe(II)-mineral pathways in Gale Crater mudstones, we conducted nucleation experiments in the Fe^{2+}-Mg^{2+}-$SiO_2(aq)$ system as a function of pH and CO_2, again under strictly anoxic conditions. As above, when its solubility is exceeded, $Fe(OH)_2$ precipitates and transforms to green rust (Fig. 2). Fe(II)-carbonates also nucleate, but at supersaturations far above those predicted by equilibrium siderite solubility (Fig. 2). In fact, our experiments delineate an apparent critical supersaturation (K_{crit}) below which metastable solutions persist without Fe(II)-carbonate nucleation (Fig. 2). This value corresponds to the solubility of amorphous Fe(II)-carbonate (AFC)[23] (Supplementary Text). The formation of AFC, a highly transient solid, offers a low energy pathway to Fe(II)-carbonate formation[26]. Upon ageing in solution, AFC may produce either siderite or chukanovite ($Fe^{II}_2(CO_3)(OH)_2$, metastable with respect to siderite[23,27]; Supplementary Text; Supplementary Figure 7).

Finally, in experiments that are supersaturated with respect to both $Fe(OH)_2$ and AFC, mixtures of green rust-CO_3, siderite, and/or chukanovite are produced (Fig. 2). Under these conditions, the kinetics of $Fe(OH)_2$ precipitation and transformation to green rust are in competition with reactions leading to Fe(II)-carbonate (eventually producing siderite). These

products are dominated by Fe(II)-carbonates relative to green rust, and green rust production becomes negligible as Fe(II)-carbonate supersaturation increases (Fig. 2).

Groundwater infiltration into a CO_2-rich lake

In contrast to recent thermodynamic models[25], our experimental observations permit high atmospheric CO_2 levels in equilibrium with the lake in Gale Crater. In the endmember case where CO_2 represented the sole acid source to the lake, two processes would have controlled steady state lake water pH: (1) buffering by atmospheric P_{CO2} and, (2) alkalinity generated from the reaction between basaltic sediments and lake water. The relative importance of these two processes is a function of the ratio between total lake water mass and the mass of sediment reacting with the lake at any one time (water/rock ratio, or W/R). Although the precise water/rock ratio is poorly constrained, regional orbital and rover-based mapping indicate that the Gale Crater lake was aerially extensive and the water column was at least several meters deep[1,2,5], suggesting that high mean water/rock ratios (i.e., >100) were likely the norm. Over the timescale of interest, kinetic calculations indicate that steady state lake water pH would have been poised between 5.2 and 5.6 at an atmospheric P_{CO2} of 1 bar and W/R ratios > 100, far below the nucleation threshold for Fe(II)-carbonate (K_{crit}) or $Fe(OH)_2$ (Fig. 2; Supplementary Text; Supplementary Figure 8). Thus, under the conditions of our simulations, lake water pH is set by the input of CO_2, formation of carbonic acid, and buffering by reaction with basaltic sediment. Calculations show that these pH conditions are sustained in the lake water body for thousands of years at all but the lowest water/rock ratios (i.e., where pH buffering by atmospheric CO_2 can be overcome by water-rock interaction; Supplementary Text; Supplementary Figure 8).

Although maximum dissolved CO_2 in the lake could have been high without precipitating Fe(II)-carbonate, geochemical and mineralogical data indicate that $Fe(OH)_2$ solubility must have been exceeded in sediments that preserve authigenic magnetite. This either requires that the entire lake body periodically experienced significant pH excursions to precipitate $Fe(OH)_2$ and eventually magnetite, or that local chemical perturbations to sedimentary pore waters drove magnetite precipitation. The topographic depression in which the Gale lake was situated resides at the lowest elevation for thousands of kilometers in any direction[2,28], and regional hydrological models predict that physical stabilization of a water body at this location involved a significant (up to 39-47% of the total influx) groundwater component[28]. Our experimental constraints on magnetite and Fe(II)-carbonate precipitation kinetics permit a quantitative test of whether groundwater infiltration and mixing with lake water could have triggered magnetite precipitation, while inhibiting Fe(II)-carbonate formation.

To evaluate the role of groundwater infiltration on authigenesis in Gale Crater mudstones, constraints on subsurface aquifer chemistry are required. On Earth, groundwater percolating through basaltic aquifers is chemically distinct from surface waters[29-31]. As meteoric water infiltrates mafic rocks, pH increases and atmospheric components are depleted along the flow path. These waters invariably become anoxic as O_2 reacts with Fe^{2+}, are devoid of dissolved CO_2 as carbonates precipitate[29-32], and commonly plateau at pH values of ~10[31,32]; Supplementary Text; Supplementary Figure 9).

With these constraints, we incorporated new experimental data for Fe(II)-mineral precipitation into a reactive transport model simulating groundwater infiltration into lacustrine sediments (Fig. 3, Supplementary Figures 10 and 11; Supplementary Text). Simulations of the diffusive transport and reaction between lake water and basaltic groundwater show that as groundwater infiltrated lacustrine sediments at Gale Crater, Fe(II)-carbonate saturation (K_{crit}) was never reached, and $Fe(OH)_2$ (eventually generating magnetite) precipitated instead (**Fig. 3,** Supplementary Figures 10 and 11). This is because groundwater raises pore water pH upon mixing, but also dilutes dissolved CO_2 derived from lake water. Time resolved simulations show that magnetite authigenesis is sustained by the release of Fe^{2+} to pore waters from olivine present in the basaltic sediment delivered to the lake, which is the most reactive silicate present in Gale Crater sediments (Supplementary Text; Figure 3, Supplementary Figures 10 and 11). Under diffusion-dominated regimes, groundwater infiltration generates observed abundances of authigenic magnetite on thousand-year timescales (Supplementary Text). Thus our modeling results show that groundwater-lake water mixing is consistent with geochemical and mineralogical data from the Sheepbed member mudstones at the base of the stratigraphic section, and deep-water mudstones of the stratigraphically higher Murray formation, both of which contain abundant authigenic magnetite[3,5,33,34].

Alkaline groundwater would have also solubilized detrital silica minerals, explaining the magnetite-silica association observed specifically in deepwater mudstones of the Murray Formation[5]. In fact, the dissolution and re-precipitation of silica polymorphs at high pH results in the formation of opal-CT in alkaline lake systems on Earth[35], providing a likely explanation for its presence in Murray mudstones.

Experimental and modeling data also show that groundwater infiltration and magnetite authigenesis at Gale Crater was accompanied by the production of $H_2(aq)$. Reactive transport simulations indicate that groundwater-lake water mixing produced $H_2(aq)$ at levels exceeding its solubility in ambient pressure aqueous solutions, therefore generating a free H_2 gas phase in the sediments (Figs. 1, 3). This result is consistent with abundant hollow nodules in Sheepbed member mudstones interpreted as voids formed by gas bubbles in the sediment during authigenesis[1,36]. In fact, the size and abundance of these nodules agrees quantitatively with the estimated volume of $H_2(g)$ produced through the decomposition of $Fe(OH)_2$ originally in the sediments (Supplementary Text).

An authigenic H_2-CO_2 mechanism for warming early Mars

Low temperature H_2 production may have a triggered a globally significant but transient feedback that warmed the early Martian surface and stabilized liquid water. Because a CO_2-rich atmosphere could not have stabilized liquid water by itself, adiabatic cooling would have transferred water ice to high altitude regions across much of the equatorial southern highlands[37,38]. This implies that topographic lows would have received liquid water through episodic melting events. As melt water permeated surface and subsurface reservoirs in low-lying regions, pulses of magnetite authigenesis would have concentrated H_2 at their interface (Figure 3, Supplementary Figure 10). Therefore, the global authigenic H_2 flux would have been proportional to the total volume of sediments hosting groundwater-surface water

mixing across the early Martian surface. Noachian to Hesperian open basin lakes represent at least ~1% of the present Martian surface[39,40], and this fraction is dominated by only a handful of lake basins located along the hemispheric dichotomy that are thought to have been groundwater-fed (on the basis of volume/catchment area)[39-41]. However, the spatial distribution of these groundwater-fed lakes is also in agreement with hydrological models that predict a shallow groundwater table in Arabia Terra and the Eridania Basin[39,41-43], which together account for at least ten percent of the Martian surface. Thus, using minimum authigenic H_2 production rates for diffusion dominated regimes (from our reactive transport simulations) and applying a constant H_2 escape rate (valid for H_2-bearing atmospheres[17]), we estimate that magnetite authigenesis alone could have led to percent-level atmospheric H_2 concentrations on early Mars if surface water-ground water mixing was sustained, on average, over 10^4 to 10^5 years or less (Figure 4). In CO_2-dominated atmospheres, these H_2 concentrations would have promoted collision-induced absorption and sufficient warming to stabilize liquid water at the early Martian surface. This positive feedback would be significantly magnified if H_2 reacted to form CH_4[16,17]. The duration of H_2-induced warming events would have been determined by H_2 escape and CH_4 photo-dissociation, restoring cold steady-state conditions through adiabatic cooling[17].

Geological data returned by the *Curiosity* rover are consistent with climatic shifts predicted by H_2-induced warming, as well as their characteristic timescales. The bulk composition of the Sheepbed member mudstone, at the base of the stratigraphic section examined by *Curiosity*, reflects low chemical index of alteration (CIA) values; these are consistent with sediment production under cold or arid climates[1,4]. Shifts to progressively higher CIA values are recorded in the overlying Murray Formation, signaling climatic conditions that supported more effective chemical denudation[5]. We predict that as H_2 gas was eventually lost from the Martian atmosphere, the lacustrine environment would have been driven to an increasingly water-limited state as liquid water stability became compromised.

Finally, H_2 produced in sedimentary systems on early Mars may have facilitated a wide range of biologically relevant chemical reactions. H_2 is an essential raw material in the synthesis of both atmospheric CH_4 and prebiotic organic compounds[44,45], and serves as a potent fuel for several autotrophic metabolisms[46]. In fact, the acetyl-CoA pathway, one of the earliest bio-energetic metabolisms on Earth[47,48], is powered by the exergonic reaction between H_2 and CO_2 – components that both accumulated at the interface between lake bottom and groundwater on early Mars. Gale Crater stratigraphy, therefore, re-defines habitability of Martian surface environments in specific chemical terms, and provides a crucial missing piece to the early Martian climate puzzle.

Methods:

Geological background of Gale Crater mudstones

Gale crater is situated in river-dissected terrain immediately south of the Martian dichotomy boundary. Gale crater formed at ~3.8-3.6 Ga[49,50], and the central portion of the crater contains sedimentary deposits that form a large mound (Mt. Sharp) that is cored by a central peak[1,49-51]. After formation, Gale Crater was infilled with alluvial fan and lacustrine sediments that were deposited and exhumed before 3.3-3.1 Ga[2,49,50,52]. The sedimentology

and stratigraphy of Gale crater sedimentary rocks are described extensively in Grotzinger et al.[1,2]; a brief summary of salient relationships is provided here. At the base of the stratigraphic section investigated by the Curiosity rover lies a thick sequence (>75 m) of mostly fluvial-deltaic sandstones and conglomerates known as the Bradbury group[53,54]. The Bradbury Group contains a basal unit, called the Yellowknife Bay formation, which is composed in part of lacustrine mudstones. These mudstones are named the Sheepbed member of the Yellowknife Bay formation. To the south of *Curiosity's* landing site, the Bradbury group interfingers with, and is ultimately overlain by, a thick sequence (>100m) of lacustrine mudstones, called the Murray formation. Both the Bradbury group and Murray fm. were buried to substantial depth (hundreds to thousands of meters), and then exhumed by eolian erosion[2]. Mudstone deposits of the Sheepbed member and the Murray fm. are predominantly composed of fine-grained rock (< 64 micron grain size) displaying massive (in the case of the Sheepbed member) to laminated (mm to cm-scale) bedding (in the case of the Murray formation), characteristic of deposition under quiescent conditions in a lake.

All mudstones examined by the Curiosity rover through ~sol 1300 contain magnetite of probable authigenic origin, in abundances ranging from 3.0-8.0 wt. %[3,5,33,34]. Potential controls on the bulk chemical composition and relative abundances of minerals and mineraloids in the mudstones of Gale Crater have been described extensively[3,5,33,34,55]. A brief summary based is provided here. The mudstone strata at Gale crater record the following sequence of events: (i) at the base of the section, in the Sheepbed member, mudstones were deposited under cold climate conditions, as evidenced by low values of the Chemical Index of Alteration (ranging from 30-37%). Sheepbed member sedimentary rocks contain detrital sulfide minerals (pyrhotite and pyrite), magnetite of probable authigenic origin, and Mg-Fe-rich smectite, all consistent with formation under anoxic conditions at neutral to alkaline pH. (ii) The stratigraphically higher Murray formation was deposited under comparatively warmer and wetter climate conditions, as evidenced by increased CIA values (ranging from 30-53%) relative to those exhibited by the Sheepbed member. The mineralogy and geochemistry of the Murray formation are consistent with deposition in a neutral-alkaline pH, redox-stratified lake environment, in which oxidized Fe-minerals (especially hematite) and phyllosilicates dominated the shallow, more oxidizing portion of the lake, while authigenic magnetite and silica were formed in anoxic waters in deeper portions of the lake.

Kinetic model of mineral dissolution

In order to investigate the influence of sediment composition on fluid chemistry in Gale Crater mudstone pore waters, we constructed a kinetic model of mineral dissolution examining the interaction of dilute water with crystalline basalt of identical composition to Rocknest, a basaltic soil deposit that was analyzed by the Curiosity rover in Gale Crater using X-ray fluorescence and X-ray diffraction techniques[56,57]. Rocknest represents an ideal starting material for our simulations because it is a recent eolian soil with a basaltic bulk composition similar to that of average Martian crust and the Sheepbed mudstones, which has experienced little chemical modification due to water-rock interaction[4]. Amorphous material reported by Blake et al.[57] was not included in the model; instead, we focus on the crystalline mineralogy, which comprises 67 wt.% of the Rocknest deposit. The amorphous component

is likely composed of a mixture of volcanic glass and poorly crystalline to amorphous mineraloids formed by alteration of that glass[55], neither of which can be reliably incorporated into a thermodynamic model of water-rock interaction. In our model, a total mass of crystalline minerals equal to 67g was multiplied by factors ranging from 0.01-100 to adjust water/rock ratios in the presence of a constant 1kg water. The model was run with Geochemists Workbench version 11[54] software, and thermodynamic data from the LLNL database[59]. Mineral dissolution rates are treated according to the general equation:

$$r = A_s k_+ a_{H+}^n \left(1 - \frac{Q}{K}\right)$$

where r is the rate of dissolution, A_S is the specific surface area, k_+ is the rate constant, a_{H+} is the dependence of the dissolution reaction on the proton concentration raised to the exponent n, and Q and K are the activity product and equilibrium constant for the dissolution reaction, respectively.

Parameters for calculating mineral dissolution rates are listed in Table S1. End member crystalline minerals were added as reactants in corresponding proportions to mineral chemistry and relative abundances for the Rocknest target reported in Blake et al.[57]. Surface areas were held constant at 1000 $cm^2\ g^{-1}$, based on an average particle size of <50 microns for mudstones in Gale Crater (from MAHLI images; 1)) and general particle size-surface area relationships for silicate minerals reported by Brantley et al.[60]. Rate constants for mixed composition silicates were calculated as weighted averages of log rate constants of the end members (as described in Brantley & Conrad[61], and then these were applied to all end members from which the rate constant was derived. In this way, realistic dissolution behavior of mixed composition silicates can be determined. Exponential pH dependencies (a_{H+}^n) were taken from Bandstra & Brantley[62]. Typical model results are depicted in Figure S1.

The results of the model show that olivine dissolution strongly affects the chemistry of initially dilute waters by releasing Mg^{2+}, $SiO_2(aq)$ and Fe^{2+} into solution more rapidly than other rock-forming silicates (Figures S1A **and** S1B). Thus, the initial chemistry of sediment pore waters will reflect this interaction. Progression of this aqueous system to alkaline pH results in supersaturation with several possible minerals, some of which are depicted in Figure S1C. This general chemical system was used as a starting point in experiments, discussed below, which examined mineral precipitation in Fe^{2+}, Mg^{2+} and SiO_2-containing systems as a function of pH and P_{CO2}. Finally, the kinetic model results predict fluid chemistries (i.e., Figure S1A) that are in quantitative agreement with water-rock interaction experiments conducted on synthetic Martian basalt of nearly identical mineralogical composition (reported in Tosca et al.[63]).

Experimental methods

Precipitation experiments were conducted to examine the competitive nucleation and growth of authigenic mineral phases that may become supersaturated in basalt-dominated sedimentary systems on Mars. Starting compositions of solutions were chosen based on

results of the kinetic model described in the previous section, an example of which is indicated in Figure S1. The interaction between fine-grained basaltic sediment and surface waters on early Mars is controlled by: the starting lithology of the basaltic material, the effective water-to-rock ratio, the initial pH, reactive surface area of sediment, and composition of the initial fluid. As discussed in the previous section, of these variables only the starting lithology of basaltic material, and, to some degree, the particle size and thus surface area, are constrained. Thus, our water-rock interaction model explores variable water-to-rock ratio (between 1 and 1000, by weight), variable initial pH (between 1 and 4) conditions. These parameters overlap with water-to-rock ratios and initial pH of experimental basalt dissolution experiments conducted by Tosca et al. (2004), and, as discussed in the text, cation concentrations are in quantitative agreement with that study, which examined fine-grained olivine-bearing basaltic material (i.e., compare Figure S1A concentrations with Figure A3E in Tosca et al., 2004). We observe that at fixed surface area and lithology, cation concentrations are controlled mainly by initial pH. In addition, the relative concentrations of the most abundant solutes (i.e., Mg^{2+}, Fe^{2+} and $SiO_2(aq)$) are essentially fixed by the presence of olivine, the most reactive rock-forming mineral in the sediment (similar to conclusions based on experiments by Tosca et al. 2004). Thus, the starting fluid compositions for experiments conducted in this study examined high, low and average total solute concentration arising from model runs (corresponding to low, high and average initial pH values examined in the model). These are: Mg^{2+}: 0.1-20 mmol/kg, Fe^{2+}: 0.04-16 mmol/kg, and $SiO_2(aq)$: 0.08-18 mmol/kg. Because initial nucleation experiments showed that that the concentrations of Mg^{2+} and $SiO_2(aq)$ relative to Fe^{2+} exerts a negligible control on the rates and mechanisms of precipitation and transformation of Fe-bearing minerals in this system, we set these three components equal to each other for the remaining experiments we pursued, some of which are reported herein.

We employed a simple chemical reactor that allowed the tracking of Fe^{2+}, Mg^{2+}, and $SiO_2(aq)$ in synthetic solutions at various fixed pH levels (Figure S2). Experiments were conducted in 1L borosilicate glass reaction vessels triple-wrapped in Al-foil (to prevent UV photolysis from fluorescent lights[64] and continuously stirred. Anoxic nucleation experiments were conducted in triplicate to assess repeatability. To maintain strictly anoxic conditions during experimentation, the vessel was housed in a Coy polymer anaerobic chamber. The anaerobic chamber was purged with a 4% H_2 / 96% N_2 gas mixture, maintaining an anoxic atmosphere through the use of a Pd catalyst and desiccant connected to a re-circulating fan box. The Pd catalyst scrubs O_2 from the system by continuously reacting trace O_2 with available H_2 in the chamber, and the resulting H_2O is then adsorbed onto a desiccant. The gas composition of the anaerobic chamber was continuously monitored with a Coy gas analyzer and the atmosphere was maintained at <1ppm $O_2(g)$ throughout the duration of all experiments and any associated sample preparation or analysis. To facilitate analysis of $H_2(aq)$ produced during the experiments, a subset of experiments was repeated after the anaerobic atmosphere was purged and replaced with ultra-pure argon. The anaerobic chamber was maintained in this condition for several days to allow purging of remnant N_2/H_2 gas mix and several process blanks were taken on de-ionized water as a comparison to solutions for which H_2 was analyzed (described below).

All aqueous solutions introduced into the anaerobic chamber were first purged of dissolved O_2 by bubbling O_2-free N_2 gas through the solution for at least 45 minutes before transfer to the glovebox[65]. Solutions were then left in the glovebox and repeatedly shaken and mixed for a further 2-3 days to allow any remaining O_2 to escape. Before experiments were started, the absence of dissolved O_2 was verified using the indigo carmine blue method[66]. Synthetic solutions were generated by the addition of relevant components (i.e., Mg, Fe, SO_4 and Cl). $SiO_2(aq)$ was added by the addition of tetraethoxysilane (TEOS), which was allowed to equilibrate in the solution for ~48 hours. Fe^{2+} was added using stock solutions that were freshly prepared prior to each experiment from de-oxygenated de-ionized water and Mohr's salt ($(NH_4)_2Fe^{2+}(SO_4)_2{\bullet}6H_2O$)). Mohr's salt is highly resistant to oxidation and was shipped from the supplier under N_2 gas and opened in the anaerobic chamber upon delivery.

In all experiments, pH was maintained at constant levels (between 7.0 and 9.0) using a Metrohm titrino 848 auto-titrator installed in the anaerobic chamber (Figure S2). Titration in these experiments was accomplished with 0.1 mmolal NaOH via a suspended tube to prevent prpecipitation at the titrant source. Rates of NaOH addition varied between a maximum of 10 mL/minute and a minimum of 10 μL/min. Some experiments also achieved constant pH through the use of the MOPS (3-(N-morpholino) propanesulfonic acid) buffer which exhibits negligible metal complexation in solution due to steric hindrance of functional groups[67].

Experiments were initiated upon titration to the desired pH level from a starting point of approximately 4. pH and oxidation reduction potential (ORP) were continuously monitored throughout the experiments. ORP was measured with a Pt electrode and was calibrated against freshly prepared ZoBell's solution[68]. This was used to periodically establish the temperature dependence of the Ag/AgCl reference electrode, and correct measured values. ORP readings were taken once values were stable to within 5 mV. Standard deviations of these readings were derived from experiments repeated in triplicate. Solution samples were withdrawn periodically and filtered through 0.1 μm nylon syringe filters in the anaerobic chamber and immediately acidified with 4% HNO_3 for subsequent elemental analysis. Solids were extracted periodically from the reactor, treated with a mini-centrifuge in the anaerobic chamber, decanted, and immediately mounted on a silicon substrate in the anaerobic chamber for powder diffraction analysis (described below). Upon experiment termination, the solution was vacuum filtered through a 0.1 μm nylon filter membrane in the anaerobic chamber. The filter and precipitate were wrapped in Al foil and allowed to dry under the low-humidity anoxic atmosphere before aliquots were taken for solid-phase analysis.

Experiments evaluating CO_2 dependence on mineral precipitation were repeated using closed borosilicate vessels with zero headspace to prevent CO_2 degassing from solution. CO_2 was added as $NaHCO_3$ which was allowed to equilibrate in solution at a given pH set by the MOPS (3-(N-morpholino) propanesulfonic acid) buffer. Experiments were started via the delivery of Fe^{2+} from stock solution by passing a syringe through a sealed septum, and were continuously shaken with an orbital shaker throughout the duration of the experiment. As above, all experiments were triple wrapped in Al foil and conducted in the anaerobic chamber.

Analytical methods

Solution analyses of major cations (Mg, Fe_T, Si) were performed via solution-phase inductively coupled plasma mass spectrometry (ICP-MS). All solutions were diluted in ultra-clean 4% HNO_3 and utilized matrix-matched element standards chosen at levels to bracket analyte concentrations.

As a consistency check and for real-time monitoring, periodic analyses of dissolved ferrous iron, total iron, SiO_2(aq) and SO_4 or Cl were performed using a HACH DR2800 bench top UV/vis spectrophotometer and the 1,10-phenanthroline, heteropoly blue and barium sulfate methods, respectively.

Once extracted in the anaerobic chamber, solid material precipitated during the experiments was analyzed by powder X-ray diffraction (XRD) using a Panalytical Empyrean diffractometer utilizing a Co Kα source, operated at 40 kV and 40 mA, and scanned between 5-65 degrees 2Θ. Powders were prepared as smears on zero background single crystal silicon substrates after centrifugation and decanting. Samples were prepared and mounted sample holders in the anaerobic chamber, and sealed with kapton foil prior to analysis, and/or treated with glycerol, both of which effectively prevented any oxidation during preparation and analysis well beyond the data collection period (less than 15 minutes).

Rietveld refinements were performed on experimental powder patterns using the GSAS-II software package[69]. Instrument parameters were determined by refining powder patterns collected under identical experimental conditions for polycrystalline Si (sample NIST 640c). Structural models for refinements of magnetite and $Fe(OH)_2$ were taken from Fleet[70] and Parise et al.[71], respectively.

H_2 analysis was conducted on a series of solution samples taken from one interval of a duplicate experiment to confirm H_2 production as indicated by electrochemistry measurements. Samples were extracted using gas-tight syringes and analyzed on a Agilent micro GC/MS equipped with a TCD/FID detector system and Ar carrier gas. Process blanks (de-ionized water collected from the reaction vessel) were run in triplicate to establish a baseline before experimental samples were run, also in triplicate. The averaged $H_2(aq)$ concentration measured in the process blanks was $33 \pm 8 \times 10^{-9}$ mol/kg.

Code availability

Two computer codes were used to generate results discussed in this manuscript: (1) Geochemist's Workbench (v11) and (2) PFLOTRAN (http://www.pflotran.org). Geochemist's Workbench is a proprietary code under copyright, maintained, and sold through Aqueous Solutions LLC; availability is not associated with this manuscript. PFLOTRAN is an open-source code available through http://www.pflotran.org. This code, utilizing thermodynamic and kinetic quantities described herein, can be used to generate results presented in this manuscript.

Data availability

The datasets generated and/or analysed during the current study are available from the corresponding author on reasonable request.

Supplementary Material

Refer to Web version on PubMed Central for supplementary material.

Acknowledgments:

We thank R.T. Pierrehumbert, A. Knoll, and J. Grotzinger for enthusiasm and feedback. N.J.T acknowledges funding from STFC grant ST/M004716/1. J.A.H. acknowledges funding from NASA grant NNX13AR09G. N.J.T. and J.A.H. thank Fondation des Treilles for support for a meeting that helped crystallize the research. We thank J. Catalano and two anonymous reviewers for comments that improved the quality of this manuscript.

References:

1. Grotzinger JP, Sumner DY, Kah LC, Stack K, et al. (2014) A Habitable Fluvio-Lacustrine Environment at Yellowknife Bay, Gale Crater, Mars. Science 343:1242777. [PubMed: 24324272]
2. Grotzinger JP, Gupta S, Malin MC, Rubin DM, et al. (2015) Deposition, exhumation, and paleoclimate of an ancient lake deposit, Gale crater, Mars. Science 350:aac7575-1–12. [PubMed: 26450214]
3. Vaniman DT, Bish DL, Ming DW, Bristow TF, et al. (2014) Mineralogy of a Mudstone at Yellowknife Bay, Gale Crater, Mars. Science 343:1243480-1–8. [PubMed: 24324271]
4. McLennan SM, Anderson RB, Bell J, Bridges J, et al. (2014) Elemental Geochemistry of Sedimentary Rocks at Yellowknife Bay, Gale Crater, Mars. Science 343:1244734-1–10. [PubMed: 24324274]
5. Hurowitz JA, Grotzinger JP, Fischer WW, McLennan SM, et al. (2017) Redox stratification of an ancient lake in Gale crater, Mars. Science 356:eaah6849. [PubMed: 28572336]
6. Ming DW, Archer PD, Glavin DP, Eigenbrode JL, et al. (2014) Volatile and Organic Compositions of Sedimentary Rocks in Yellowknife Bay, Gale Crater, Mars. Science 343:1245267-1–9. [PubMed: 24324276]
7. Bristow TF, Bish DL, Vaniman DT, Morris RV, et al. (2015). The origin and implications of clay minerals from yellowknife bay, gale crater, mars. American Mineralogist, 100: 824–836. doi: 10.2138/am-2015-5077CCBYNCN [PubMed: 28798492]
8. Pollack JB, Kasting JF, Richardson SM, and Poliakoff K (1987) The case for a wet, warm climate on early Mars. Icarus 71:203–224. [PubMed: 11539035]
9. Kasting JF (1991) CO_2 condensation and the climate of early Mars. Icarus 94:1–13. [PubMed: 11538088]
10. Forget F, Wordsworth R, Millour E, Madeleine J, et al. (2013) 3D modelling of the early martian climate under a denser CO_2 atmosphere: Temperatures and CO_2 ice clouds. Icarus 222:81–99.
11. Postawko SE, and Kuhn WR (1986) Effect of the greenhouse gases (CO_2, H_2O, SO_2) on Martian paleoclimate. Journal of Geophysical Research: Solid Earth 91:431–438.
12. Halevy I, Zuber MT, and Schrag DP (2007) A sulfur dioxide climate feedback on early Mars. Science 318:1903. [PubMed: 18096802]
13. Halevy I, and Head III JW (2014) Episodic warming of early Mars by punctuated volcanism. Nature Geosci 7:865–868.
14. Mischna MA, Baker V, Milliken R, Richardson M, and Lee C (2013) Effects of obliquity and water vapor/trace gas greenhouses in the early martian climate. Journal of Geophysical Research: Planets 118:560–576.
15. Kerber L, Forget F, and Wordsworth R (2015) Sulfur in the early martian atmosphere revisited: Experiments with a 3-D Global Climate Model. Icarus 261:133–148.

16. Ramirez RM, Kopparapu R, Zugger ME, Robinson TD, Freedman R, and Kasting JF (2013) Warming early Mars with CO2 and H2. Nature Geoscience 7:59–63.
17. Wordsworth R, Kalugina Y, Lokshtanov S, Vigasin A, Ehlmann B, Head J, Sanders C, and Wang H (2017) Transient reducing greenhouse warming on early Mars. Geophysical Research Letters 44:665–671.
18. Hirschmann MM, and Withers AC (2008) Ventilation of CO_2 from a reduced mantle and consequences for the early Martian greenhouse. Earth and Planetary Science Letters 270:147–155.
19. Chassefiere E, Langlais B, Quesnel Y, and Leblanc F (2013) The fate of early Mars' lost water: The role of serpentinization. Journal of Geophysical Research: Planets, 118: 1123–1134.
20. Ehlmann BL, Mustard JF, and Murchie SL (2010) Geologic setting of serpentine deposits on Mars. Geophysical Research Letters, 37: L0621.
21. Syverson DD, Tutolo BM, Borrok DM, and Seyfried WE (2017) Serpentinization of olivine at 300°C and 500 bars: An experimental study examining the role of silica on the reaction path and oxidation state of iron. Chemical Geology, 475, 122–134.
22. Tutolo BM, Luhmann AJ, Tosca NJ, and Seyfried WE (2018) Serpentinization as a reactive transport process: The brucite silicification reaction. Earth and Planetary Science Letters, 484, 385–395.
23. Dideriksen K, Frandsen C, Bovet N, Wallace AF, et al. (2015) Formation and transformation of a short range ordered iron carbonate precursor. Geochimica et Cosmochimica Acta 164:94–109.
24. Tosca NJ, Guggenheim S, and Pufahl PK (2016) An authigenic origin for Precambrian greenalite: Implications for iron formation and the chemistry of ancient seawater. Geological Society of America Bulletin 128:511–530.
25. Bristow TF, Haberle RM, Blake DF, Des Marais DJ, et al. (2017) Low Hesperian P_{CO2} constrained from in situ mineralogical analysis at Gale Crater, Mars. Proceedings of the National Academy of Sciences 114: 201616649.
26. Sel O, Radha AV, Dideriksen K, and Navrotsky A (2012) Amorphous Iron (II) Carbonate: Crystallization Energetics and Comparison to Other Carbonate Minerals related to CO_2 Sequestration. Geochimica et Cosmochimica Acta 87:61–68.
27. Azoulay I, Rémazeilles C, and Refait P (2012) Determination of standard Gibbs free energy of formation of chukanovite and Pourbaix diagrams of iron in carbonated media. Corrosion Science 58:229–236.
28. Horvath DG, and Andrews-Hanna JC (2017) Reconstructing the past climate at Gale crater, Mars, from hydrological modeling of late-stage lakes. Geophysical Research Letters 44:8196–8204.
29. Gislason SR, and Eugster HP (1987) Meteoric water-basalt interactions. II: A field study in NE Iceland. Geochimica et Cosmochimica Acta 51:2841–2855.
30. Stefansson A, Gislason SR, and Arnorsson S (2001) Dissolution of primary minerals in natural waters II. Mineral saturation state. Chemical Geology 172:251–276.
31. Arnórsson S, Gunnarsson I, Stefánsson A, Andrésdóttir A, and Sveinbjörnsdóttir E (2002) Major element chemistry of surface-and ground waters in basaltic terrain, N-Iceland: I. primary mineral saturation. Geochimica et Cosmochimica Acta 66:4015–4046.
32. Barnes I, and O'Neil JR (1969) The relationship between fluids in some fresh alpine-type ultramafics and possible modern serpentinization, western United States. Geological Society of America Bulletin 80:1947–1960.
33. Morris RV, Vaniman DT, Blake DF, Gellert R, et al. (2016) Silicic volcanism on Mars evidenced by tridymite in high-SiO_2 sedimentary rock at Gale crater. Proceedings of the National Academy of Sciences 113:7071–6.
34. Rampe EB, Ming DW, Blake DF, Bristow TF, et al. (2017) Mineralogy of an ancient lacustrine mudstone succession from the Murray formation, Gale crater, Mars. Earth and Planetary Science Letters 471:172–185.
35. Renaut RW, Tiercelin JJ, and Owen RB (1986) Mineral precipitation and diagenesis in the sediments of the Lake Bogoria basin, Kenya Rift Valley. Geological Society, London, Special Publications 25:159–175.

36. Stack M, Grotzinger JP, Kah LC, Schmidt ME, et al. (2014) Diagenetic origin of nodules in the Sheepbed member, Yellowknife Bay formation, Gale Crater, Mars. Journal of Geophysical Research: Planets 119:1637–1664.
37. Wordsworth R, Forget F, Millour E, Head JW, Madeleine J, and Charnay B (2013) Global modelling of the early martian climate under a denser CO_2 atmosphere: Water cycle and ice evolution. Icarus 222:1–19.
38. Wordsworth RD, Kerber L, Pierrehumbert RT, Forget F, and Head JW (2015) Comparison of "warm and wet" and "cold and icy" scenarios for early Mars in a 3-D climate model. J. Geophys. Res. Planets 120:1201–1219.
39. Fassett CI, and Head JW (2008) Valley network-fed, open-basin lakes on Mars: Distribution and implications for Noachian surface and subsurface hydrology. Icarus 198:37–56.
40. Goudge TA, Head JW, Mustard JF, and Fassett CI (2012) An analysis of open-basin lake deposits on Mars: Evidence for the nature of associated lacustrine deposits and post-lacustrine modification processes. Icarus 219:211–229.
41. Irwin RP, Maxwell TA, Howard AD, Craddock RA, and Leverington DW (2002) A large paleolake basin at the head of Ma'adim Vallis, Mars. Science 296:2209–12. [PubMed: 12077414]
42. Andrews-Hanna JC, Zuber MT, Arvidson RE, and Wiseman SM (2010) Early Mars hydrology: Meridiani playa deposits and the sedimentary record of Arabia Terra. J. Geophys. Res 115:E06002.
43. Andrews-Hanna JC, and Lewis KW (2011) Early Mars hydrology: 2. Hydrological evolution in the Noachian and Hesperian epochs. Journal of Geophysical Research 116:E02007.
44. Abelson PH (1966) Chemical events on the primitive Earth. Proceedings of the National Academy of Sciences 55:1365–1372.
45. Miller SL (1953) A production of amino acids under possible primitive earth conditions. Science 117:528–529. [PubMed: 13056598]
46. Canfield DE, Kristensen E, and Thamdrup B (2005) Aquatic Geomicrobiology (Elsevier, Amsterdam), pp. 636.
47. Ragsdale SW, and Pierce E (2008) Acetogenesis and the Wood-Ljungdahl pathway of CO_2 fixation. Biochimica et Biophysica Acta (BBA)-Proteins and Proteomics 1784:1873–1898. [PubMed: 18801467]
48. Braakman R, and Smith E (2012) The emergence and early evolution of biological carbon-fixation. PLoS Comput Biol 8:e1002455. [PubMed: 22536150]
49. Thomson BJ, Bridges NT, Milliken R, Baldridge A, et al. (2011) Constraints on the origin and evolution of the layered mound in Gale Crater, Mars using Mars Reconnaissance Orbiter data. Icarus 214:413–432.
50. Le Deit L, Hauber E, Fueten F, Pondrelli M, Rossi AP, and Jaumann R (2013) Sequence of infilling events in Gale Crater, Mars: Results from morphology, stratigraphy, and mineralogy. Journal of Geophysical Research: Planets 118:2439–2473.
51. Palucis MC, Dietrich WE, Hayes AG, Williams RME, et al. (2014) The origin and evolution of the Peace Vallis fan system that drains to the Curiosity landing area, Gale Crater, Mars. Journal of Geophysical Research: Planets 119:705–728.
52. Grant JA, Wilson SA, Mangold N, Calef F, and Grotzinger JP (2014) The timing of alluvial activity in Gale crater, Mars. Geophysical Research Letters 41:1142–1149.
53. Szabó T, Domokos G, Grotzinger JP, and Jerolmack DJ (2015) Reconstructing the transport history of pebbles on Mars. Nat Commun 6:8366. [PubMed: 26460507]
54. Williams RME, Grotzinger P, Dietrich E, Gupta S, et al. (2013) Martian Fluvial Conglomerates at Gale Crater. Science 340:1068–1072. [PubMed: 23723230]
55. Dehouck E, McLennan SM, Meslin P, and Cousin A (2014) Constraints on abundance, composition, and nature of X-ray amorphous components of soils and rocks at Gale crater, Mars. J. Geophys. Res. Planets 119:2640–2657.
56. Bish DL, Blake DF, Vaniman DT, Chipera SJ, et al. (2013) X-ray Diffraction Results from Mars Science Laboratory: Mineralogy of Rocknest at Gale Crater. Science 341:1238932. [PubMed: 24072925]

57. Blake DF, Morris RV, Kocurek G, Morrison SM, et al. (2013) Curiosity at Gale Crater, Mars: Characterization and Analysis of the Rocknest Sand Shadow. Science 341:1239505. [PubMed: 24072928]
58. Bethke CM, and Yeakel S (2017) The Geochemist's Workbench, *Release 11.0* (Aqueous Solutions LLC).
59. Delany JM, and Lundeen SR (1990) The LLNL thermochemical database. 150pp.
60. Brantley SL, White AF, and Hodson ME (1999) in *Growth, Dissolution and Pattern Formation in Geosystems*, editor Jamtveit B, and Meakin P (Kluwer, Dordrecht), p 291–326.
61. Brantley SL, and Conrad CF (2008) in Kinetics of water-rock interaction (Springer), p 1–37.
62. Bandstra JZ, and Brantley SL (2008) in Kinetics of Water-Rock Interaction (Springer), p 211–257.
63. Tosca NJ, McLennan SM, Lindsley DH, and Schoonen MAA (2004) Acid-sulfate weathering of synthetic Martian basalt: The acid fog model revisited. Journal of Geophysical Research - Planets 109:doi:10.1029/2003JE002218.
64. Braterman PS, Cairns-Smith AG, and Sloper RW (1984) Photo-oxidation of iron(II) in water between pH 7.5 and 4.0. Journal of the Chemical Society, Dalton Transactions:1441–1445.
65. Butler IB, Schoonen MA, and Rickard DT (1994) Removal of dissolved oxygen from water: a comparison of four common techniques. Talanta 41:211–215. [PubMed: 18965910]
66. Loomis WF (1954) Rapid Microcolorimetric Determination of Dissolved Oxygen. Anal Chem 26:402–404.
67. Kandegedara A, and Rorabacher DB (1999) Noncomplexing Tertiary Amines as "Better" Buffers Covering the Range of pH 3-11. Temperature Dependence of Their Acid Dissociation Constants. Anal Chem 71:3140–4. [PubMed: 21662904]
68. Nordstrom DK (1977) Thermochemical redox equilibria of ZoBell's solution. Geochimica et Cosmochimica Acta 41:1835–1841.
69. Toby BH, and Von Dreele RB (2013) GSAS-II: the genesis of a modern open-source all purpose crystallography software package. Journal of Applied Crystallography 46:544–549.
70. Fleet ME (1986) The structure of magnetite: Symmetry of cubic spinels. Journal of Solid State Chemistry 62:75–82.
71. Parise JB, Marshall WG, Smith RI, Lutz HD, and Möller H (2000) The nuclear and magnetic structure of white rust $Fe(OH_{0.86}D_{0.14})_2$. American Mineralogist 85:189–193.

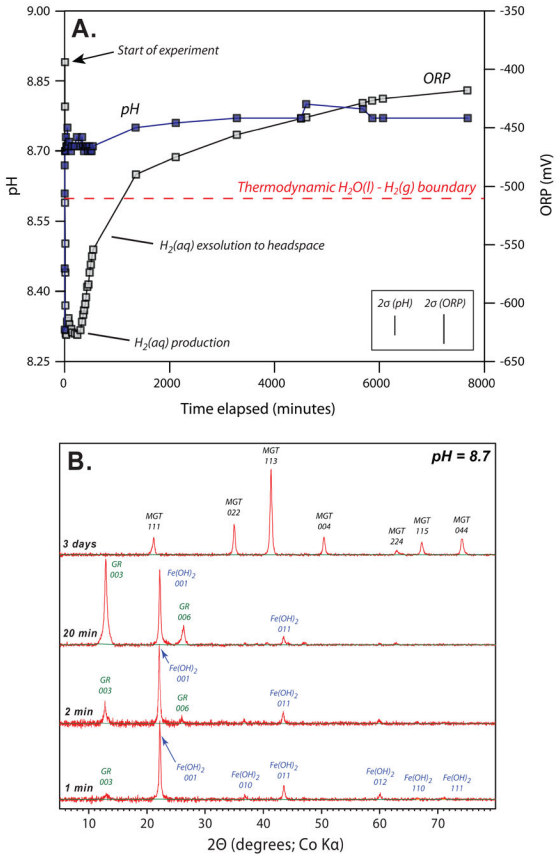

Fig. 1.

Anoxic precipitation experiment with Mg^{2+}, Fe^{2+}, and $SiO_2(aq)$ bearing water. **(A.)** As pH is increased oxidation-reduction potential (ORP) falls below the thermodynamic stability of $H_2O(l)$, as $H_2(aq)$ is generated, which then slowly degasses to the reactor headspace. **(B.)** Under strictly anoxic conditions, pH increases precipitate $Fe(OH)_2$ which rapidly converts to green rust, in turn reducing $H_2O(l)$ and forming $H_2(aq)$. Metastable green rust transforms to magnetite in days. Error bars denote 2σ derived from triplicate experiments.

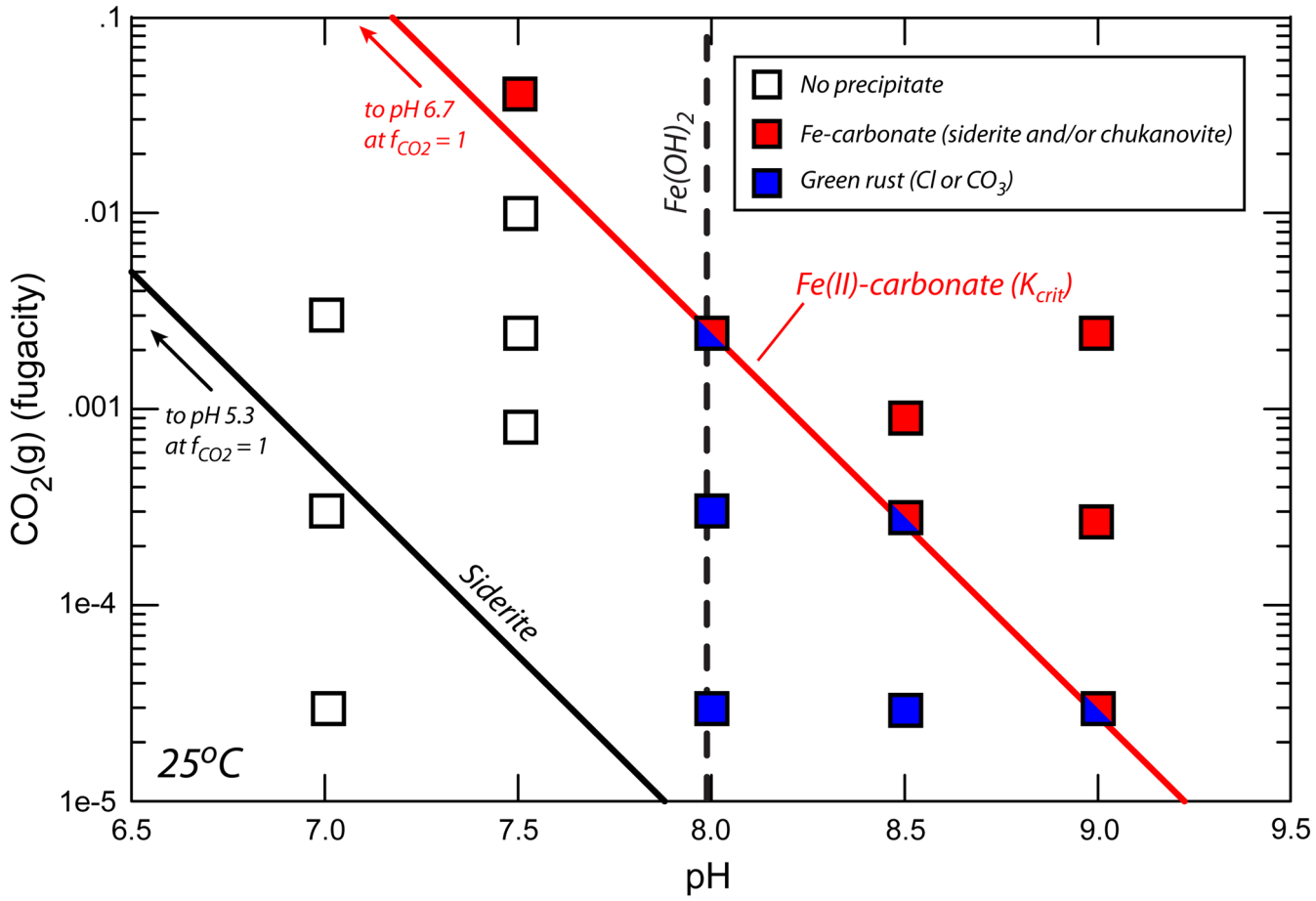

Fig. 2.

Anoxic precipitation experiments as a function of pH and dissolved CO_2. Water compositions initially supersaturated with respect to $Fe(OH)_2$ (to the right of the blue dashed line) generate green rust through the transformation shown in Figure 1. Compositions initially supersaturated with respect to siderite (above the black line) do not generate Fe(II)-carbonate unless a critical supersaturation value (red line; K_{crit}) is crossed. Compositions supersaturated with respect to both Fe(II)-carbonate and $Fe(OH)_2$ yield mixtures of Fe(II)-carbonate and green rust; products are dominated by the former as supersaturation increases. 2σ derived from triplicate experiments is smaller than the symbols.

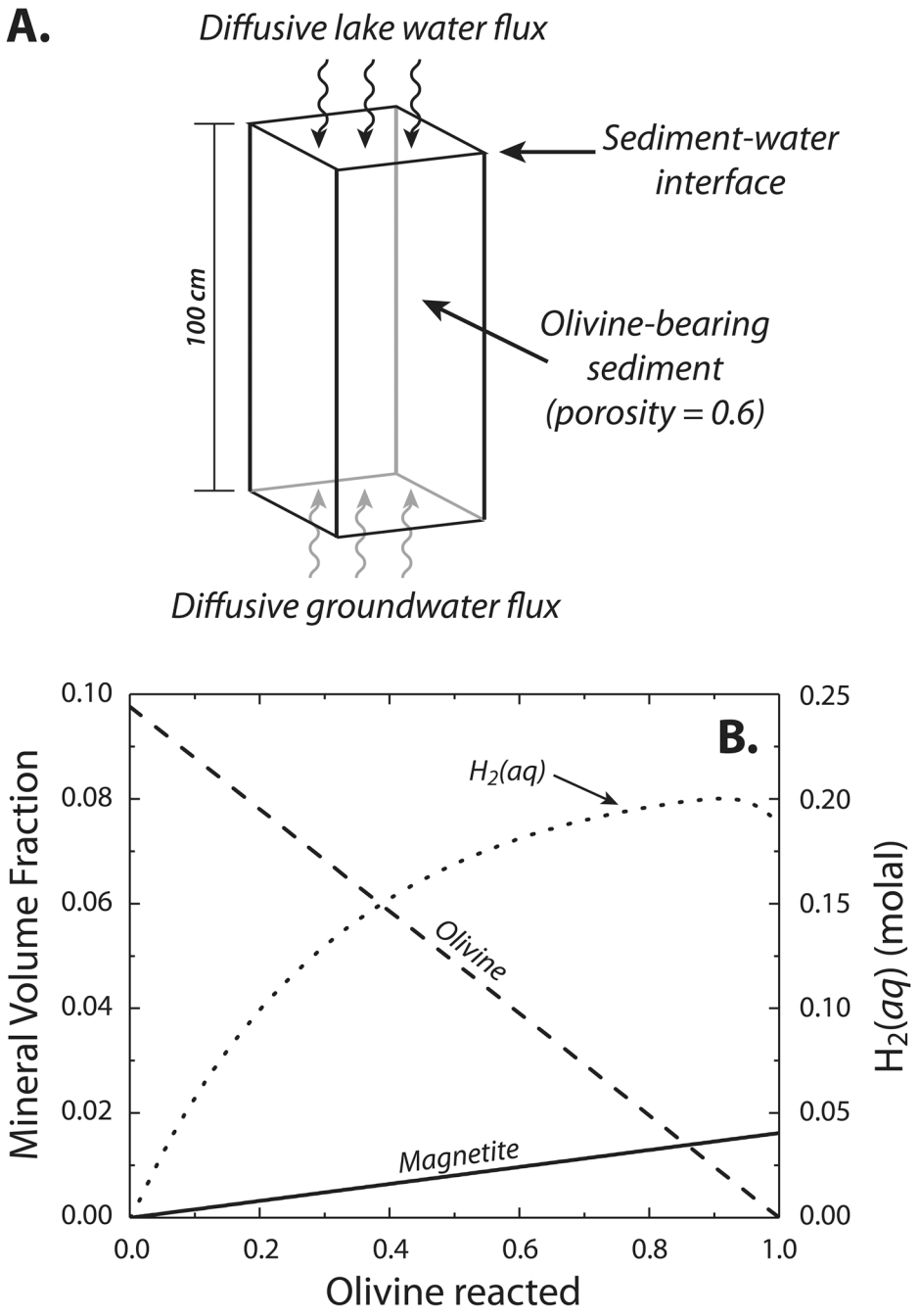

Fig. 3.

Ground water-lake water mixing to form magnetite and H_2 (*aq*). **(A.)** Schematic of domain used in reactive transport simulations. **(B.)** Mineral volume fraction and H_2 (*aq*) concentrations in coexisting solutions plotted as a function of olivine reaction progress. Note that H_2 (*aq*) concentrations plotted here exceed the solubility of H_2(*aq*) in ambient-pressure solutions, and would be expected to generate a free gas phase within the sediments. The curvature in H_2 (*aq*) is related to the diminishing reactivity of olivine as its volume fraction is depleted, and the increased diffusional gradient of H_2 (*aq*) out of the domain.

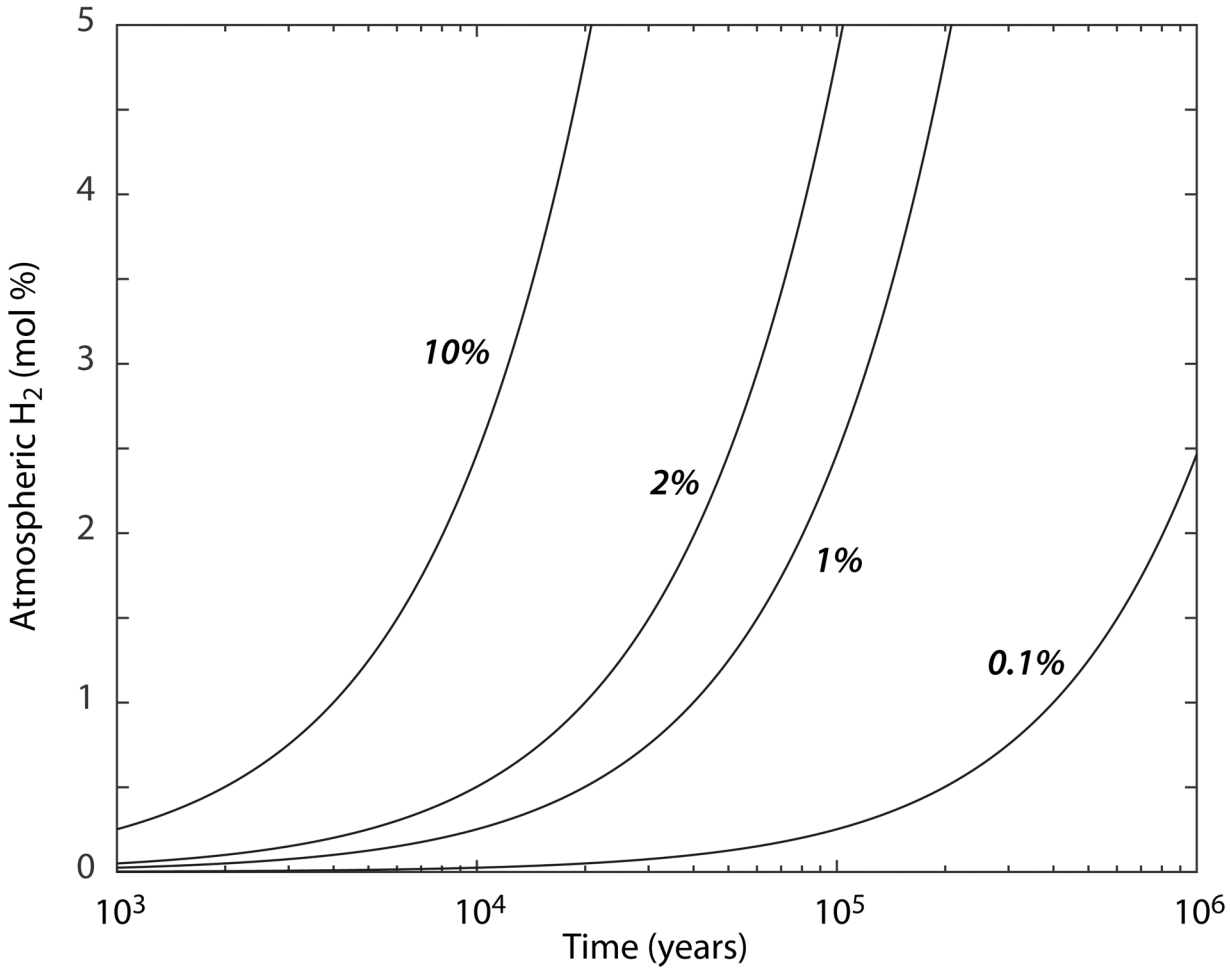

Fig. 4.

Globally averaged authigenic H_2 production on early Mars. As surface and subsurface water reservoirs interact on early Mars and trigger authigenic magnetite precipitation, atmospheric H_2 concentration increases to percent levels over timescales of 10^4 to 10^5 years or less. Lines indicate atmospheric H_2 concentrations calculated at various percentages of the early Martian surface hosting authigenic H_2 production. Calculations apply a constant H-escape rate for H_2-bearing atmospheres[17].